agriculture

MDPI

Article

CFD–DEM Analysis and Field Evaluation of a Dual-Roller Fresh-Safflower Filament Harvester with Pneumatic-Assisted Separation

Zhenghao Wang [1], Zhan Zhao [1,*], Qianqian Zhou [1], Yun Ge [2], Yijiang Zheng [2] and Zhen Xue [3]

[1] School of Agricultural Engineering, Jiangsu University, Zhenjiang 212013, China; 2212416035@stmail.ujs.edu.cn (Z.W.); 2112216013@stmail.ujs.edu.cn (Q.Z.)
[2] College of Mechanical and Electrical Engineering, Shihezi University, Shihezi 832003, China; gy_mac@shzu.edu.cn (Y.G.); zyj202200152@shzu.edu.cn (Y.Z.)
[3] Taizhou Xiechuang Agricultural Equipment Co., Ltd., Taizhou 225312, China; 19708897339@163.com
* Correspondence: zhaozhan@ujs.edu.cn

Abstract

To achieve the efficient mechanized harvesting of fresh safflower filaments, this paper proposes a harvesting device using dual-roller gripping and pneumatic-assisted separation. According to the mechanical properties of fresh filaments, the meta-particle method is employed to construct a flexible geometric model, and the Edinburgh elasto-plastic adhesion (EEPA) contact model is used to calculate the contact forces. It is found that, as the dual-roller gap decreases, the maximum normal contact force and adhesive force increase according to power law relationships. The increased adhesion can cause filaments to remain on the roller surfaces, resulting in adhesion-induced carry-back. Then, CFD–DEM coupling simulations are carried out to analyze filament gripping and transportation. The results reveal that two air jets at a pressure difference of 1.0 kPa assist filament separation from the roller surfaces. Finally, a harvesting machine is developed, and comparative field tests are carried out. At a dual-roller gap of 0.8 mm, a rotational speed of 800 rpm and a pressure difference of 1.0 kPa, the filament pulling-out rate and effective collection rate are 91.4 ± 0.6% and 84.3 ± 0.2%, respectively (mean ± standard deviation across three spatial sampling sections within one field pass). These results support pneumatic-assisted separation under the tested conditions.

Keywords: fresh safflower filaments; harvesting device; pneumatic-assisted separation; dynamic analysis; CFD–DEM coupling simulation

Check for updates

Academic Editor: Eglė Jotautienė

Received: 7 September 2026
Revised: 9 October 2026
Accepted: 14 October 2026
Published: 15 October 2026

Copyright: © 2026 by the authors. Licensee MDPI, Basel, Switzerland. This article is an open access article distributed under the terms and conditions of the Creative Commons Attribution (CC BY) license.

1. Introduction

Safflower is a versatile crop with great economic value that is widely cultivated in East Asia, Central Asia, and North America [1,2]. Its filaments are traditional Chinese medicinal herbs and health-promoting ingredients, while the seeds are an important source of high-quality cooking oil [3–5]. With the breakthrough in the extraction process of safflower pigments, the demand for filament raw materials has been growing rapidly. There are two methods for harvesting safflower filaments: fresh filaments and dried filaments. After fresh safflower filaments are naturally dried, their chemical composition changes, and the content of key active ingredients, such as hydroxysafflor yellow A, can decrease, thereby affecting their quality [6]. The harvesting of fresh safflower filaments is highly time-sensitive. The flowering time of safflower is inconsistent and the peak flowering period is short; as a

result, one field usually requires to be harvested two to three times at intervals of 3 to 4 days [1,7]. Currently, this harvesting work still relies primarily on manual labor, with high labor intensity and manual harvesting costs exceeding 50% of the returns from safflower cultivation. This reliance on manual labor has become a major obstacle restricting the efficient development of the safflower industry [8,9].

The technical requirements for harvesting fresh safflower filaments are relatively high. It is essential to avoid damaging the filaments or flower bulbs, as damaged filaments will reduce their value, while the flower bulbs need to continue growing to increase the content of safflower seed oil. To achieve mechanized harvesting of fresh safflower filaments, scholars have explored various harvesting methods such as using pneumatic, cutting and pulling techniques, and have designed various end-effectors. Steberl et al. [9] investigated combine harvesting of safflower florets in Germany, considering cultivar, harvest date and threshing settings. This approach enabled mechanical floret recovery, although the harvested material contained leaves and branches and required further sieving. Azimi et al. [10] developed a pneumatic harvester that uses fan suction to detach and convey safflower petals without mechanical cutting. However, because the airflow performs both detachment and transportation, its operating conditions must satisfy both functions. These approaches show that the harvesting mechanism needs to be considered together with the subsequent separation and collection process. Zhang et al. [11,12] designed two types of end-effectors using the cutting principle: the rotary shearing type and the dual-translational cutting type. When the filaments are detected entering the picking gate, the blades are activated to perform the cutting operation. The structure of the component is complex, and can only be operated manually to pick up filaments from an individual flower bulb. Han et al. [13] and Huang et al. [14] designed a pneumatic-cutting-type safflower filament harvesting device. They added the negative-pressure airflow to make the filaments at the cutting point stand upright, then used a rotating cutter to cut the bottom of the filaments, thereby improving the harvesting rate. Liu et al. [15] optimized the combination of negative pressure airflow field and cutting parameters through comparative experiments. Based on the mechanical properties of the filaments, Chen et al. [16] proposed a biomimetic design for a cutting blade. Although pneumatic assistance and bionic blade design can improve cutting performance, filament damage remains sensitive to the blade geometry, rotational speed and airflow conditions. In addition, He et al. [17] simulated the manual grasping and pulling motions, and then designed a guide rail pulling-type harvesting device. Yang et al. [18] designed a flexible harvesting device using a three-fingered robotic gripper. Compared with cutting, gripping and pulling mechanisms avoid blade-induced severing of the filaments. However, they require coordinated gripping, pulling and release motions, making effective feeding and motion coordination important for successive harvesting operations [17,18].

The dual-roller gripping method is a technique that simulates manual harvesting [19,20]. Based on the slender shape and light weight of safflower filaments, a pair of rollers rotating in opposite directions exert friction and compression forces, thereby pulling out filaments from the flower bulbs. The rotating dual rollers can also comb the filaments, so it does not require very precise positioning of the flower bulb or the control of gripping motion. Ge et al. [21] designed a handheld harvesting component, and optimized the structural and operational parameters such as the rotational speed and gap of the dual rollers. Zhang et al. [22] added a negative pressure fan to the mechanical structure, and used the negative pressure airflow field to enhance the transportation of the extracted filaments into the collection bins. The application of sufficient pressure to the filaments by the dual rollers is the key to ensuring effective gripping performance. The moisture content of fresh safflower filaments in the mature stage is usually over 60%. Under the high temperatures

of summer, the filaments are prone to sticking to the surfaces of the rotating rollers when they are subjected to pressure, resulting in repeated crushing, backtracking and falling into the field, and even blocking the rollers. This is a phenomenon that commonly occurs while using the dual-roller gripping method.

Previous studies have mainly focused on the structural design and operating characteristics of harvesting components. The efficiency of harvesting safflower filaments using a handheld component is very low. Some attempts have been made by using a CCD camera to locate the positions of the flower bulbs, and then cutting the bottom of the filaments using a parallel robot arm. The average harvesting time for a single flower bulb exceeds 10 s, and the stability is still very poor due to the complex and significantly varied morphology of the safflower plants [23]. The dual-roller gripping method has been preliminarily proven to be an effective way for harvesting fresh safflower filaments. Wang et al. [24] investigated plant feeding and coordinated canopy coverage in a parallel multi-picking-head harvesting system jointly developed with the present research team. However, sufficient gripping does not ensure that the pulled filaments are released from the roller surfaces, as the applied pressure may also increase residual adhesion and carry-back. The relationship between gripping and subsequent release therefore requires further clarification, particularly the role of auxiliary airflow in promoting separation while maintaining effective gripping. The essence is to analyze the dynamic behavior of the flexible and viscous filaments under the coupled effects of the gripping force exerted by rotating dual rollers and the separation force generated by the airflow field [25,26]. After decades of development, the CFD–DEM coupling simulation has become an established approach for studying fluid–particle systems [27–29]. By introducing bond key connection technology, the particle form expands from initial solid particles to flexible bodies [30]. The bonds can be stretched, bent or twisted, thereby simulating the deformation of a flexible body. When the applied force exceeds the strength limit of the bonds, they will break, thereby simulating the fragmentation of the flexible body [31,32]. Schramm and Tekeste [33] combined the multi-sphere assembly method with the fiber-bonding model to establish a highly flexible discrete element model for simulating the mechanical properties of wheat straw, and accurately calibrated the microscopic bonding stiffness and critical fracture stress of the straw. Korn and Herlitzius [34] employed the CFD–DEM coupling method to numerically simulate the separation process in combine harvester cleaning devices using rigid multi-sphere particles. They evaluated the simulation results by comparison with separation experiments. Xu et al. [35] established non-spherical agricultural particles and verified the reliability of CFD–DEM simulations in predicting the performance of complex pneumatic transportation and separation. Nowadays, the dynamic behavior of flexible bodies in fluid fields is still an important theoretical topic and a cutting-edge direction in the CFD–DEM coupling simulation research field [36,37].

This paper proposes a pneumatic-assisted separation method for the dual-roller harvesting system to facilitate filament release after pulling. While retaining the existing rubber-strip cleaning structure, localized air jets are introduced on both sides of the rollers to assist the separation of adhered filaments and reduce carry-back. The coupled gripping, adhesion and separation processes are investigated to determine the operating conditions required for effective filament pulling and subsequent release. The main contributions of this study can be summarized as follows. (1) The structure of a harvesting component combining dual-roller gripping and pneumatic-assisted separation is designed. (2) The critical conditions for effectively pulling the filaments from the flower bulb and separating them from the rotating roller surfaces are formulated. (3) The filament harvesting dynamics are investigated through CFD–DEM coupling simulations, and suitable operating parameters are identified within the investigated range. (4) A safflower filament harvesting

machine is developed, and comparative field tests with and without pneumatic assistance are carried out.

2. Materials and Methods

2.1. Properties of Safflower

The properties of mature safflower flowers, flower bulbs and filaments are the basis for designing harvesting devices. A typical safflower plant cultivated in the Xinjiang region of China is shown in Figure 1. Published measurements [24,38,39] were used as references for the morphological description and the selection of model parameters.

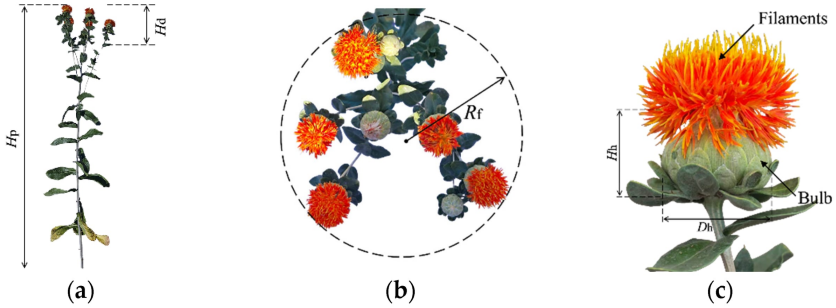


Figure 1. Morphological characteristics of mature safflowers. (**a**) Mature safflower plant; (**b**) Safflower plant width; (**c**) safflower head.

Safflower is a type of multi-branched plant of the Asteraceae family. Its flower bulbs are primarily distributed throughout the canopy, exhibiting a certain irregularity and dispersion in spatial distribution. The average plant height H_p is about 600 to 700 mm, and the height range of the flower bulbs H_d is about 80 to 140 mm. The radius R_f of the area where the flower bulbs are distributed on the horizontal plane is about 125 mm. The shape of the flower bulb is an elliptical body with a narrow top and a wide bottom. The average diameter D_h is about 25 mm and the height H_h is about 20 mm [24,38]. During the initial 1 to 2 days of safflower blooming, the moisture content of the filaments ranges from 76.6 to 78.4%. The moisture content will gradually decrease to the range of 44.6 to 65.8% at full bloom. The length of the filaments L can reach about 12 to 25 mm. The mass of a cluster of filaments is about 2 to 2.5 g. Ge et al. [38] measured the separation force F_s required to detach the filaments from the flower bulb using a tension sensor and reported a range of 7.66–13.06 N. The material, aerodynamic and contact parameters used in this study are summarized in Table 1. The sources and selection methods of the mechanical model parameters are described in Section 2.3.

Table 1. Material, aerodynamic and contact parameters used in this study.

Property Category	Parameter	Filament	Dual Rollers
Material property	Density (kg/m^3)	400 [a]	1150 [c]
	Poisson's ratio (-)	0.25 [a]	0.49 [c]
	Shear modulus (MPa)	1.0 [a]	28 [c]
Aerodynamic property	Suspension velocity (m/s)	1.59−2.91 [d]	/
Contact-pair property	Coefficient of restitution	0.15 [a]	0.35 [b]
	Static friction coefficient	0.57 [a]	0.70 [b]
	Rolling friction coefficient	0.20 [a]	0.6 [b]

[a] Literature-derived inputs adopted from Zhang et al. [39]; the applicability of the Poisson's ratio and shear modulus to the filament model is discussed in Section 2.3. [b] Obtained through the phenomenological calibration described in Section 2.3. [c] Prescribed model inputs, held constant during calibration. [d] Reported by Ge et al. [38] for filaments sampled on days 1–8 after flowering. For contact-pair properties, the "Filament" and "Dual roller" columns refer to filament–filament and filament–roller contacts, respectively.

2.2. Structure of Harvesting Component

The structure of the harvesting component is shown in Figure 2. Its total length, width and height are 455 mm, 360 mm, and 210 mm, respectively. Three sets of dual rollers are installed in parallel for each harvesting component to increase the contact area between the harvesting component and the safflower canopy, with the aim of improving harvesting efficiency and harvesting rate. The dual rollers are driven through a synchronous belt by a motor (ACL60200S5-2500M-24-14, Shenzhen Dayond Factory Automation Control System Co., Ltd., Shenzhen, China) with a rated voltage of 24 V DC, a rated power of 200 W, a rated current of 12 A and a rated speed of 3000 rpm. The rated and peak motor torques are 0.637 and 1.91 N·m, respectively. The motor-side and roller-side synchronous pulleys have 18 and 15 teeth, respectively, resulting in a roller speed 1.2 times the motor output-shaft speed. The two rollers rotate in opposite directions at the same speed, and the roller speed can be adjusted within the range of 600 to 1200 rpm. According to the geometric dimensions and distribution characteristics of the flower bulbs, the roller is designed with a diameter of 30 mm and a length of 300 mm. The dual-roller gap can be adjusted within the range of 0–2 mm. The distance between two adjacent sets of dual rollers is 85 mm. The rollers are made of polyurethane rubber with a hardness of 90 Shore A. The roller surfaces directly contact the filaments and have a raised pattern of 0.5 mm height to facilitate gripping.

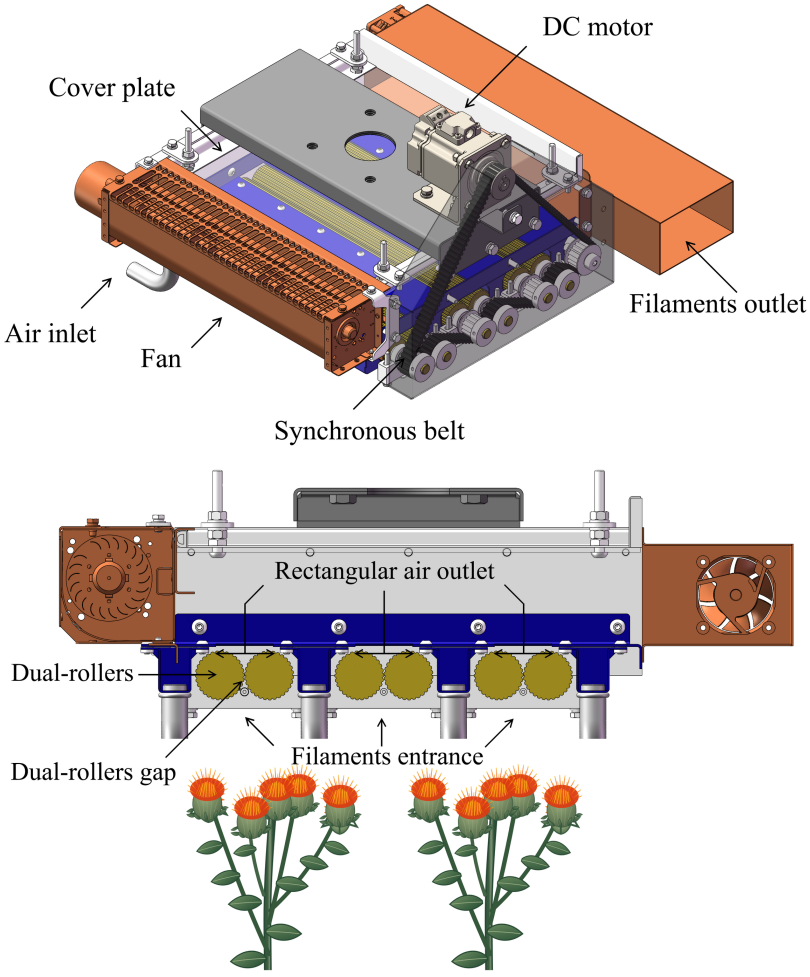


Figure 2. Structure of harvesting component. (**top**) Harvesting unit; (**bottom**) Cross-section of the harvesting unit and harvesting schematic.

There are three filament entrances, which are located below the intersecting lines of the dual rollers. The bottom plate and upper cover plate form a conveying channel. Each

harvesting component is equipped with two cross-flow fans installed on the two sides of the channel to generate the conveying airflow. Cross-flow fans were selected because they can form a relatively stable airflow region with a comparatively uniform velocity distribution along the axial direction [40], which is favorable for maintaining airflow coverage across the conveying channel. Each fan operates at 24 V, with a specified pressure of 45 Pa and an airflow rate of 260 m^3/h. Four rectangular positive-pressure air chambers are installed below the bottom plate. Each chamber is 17 mm long, 26 mm high and 300 mm deep. Three rectangular air slits are arranged on each of its two opposite sides, giving six slits per chamber. Each slit is 60 mm long and 0.5 mm wide, thereby generating jet airflow on both sides of the dual rollers. The directions of the jet flow fields are toward the corresponding filaments entrances.

Each harvesting component is suspended on the frame by an independent electric cylinder. During harvesting operations, the electric cylinder drives the component to perform reciprocating motion in the vertical direction, with a stroke of 150 mm and a complete reciprocating cycle of 2.7–3.5 s. When the rotating dual rollers come into contact with the flower bulbs, the filaments will be pulled away from the bulbs, and gripped upward through the dual-roller gap. Subsequently, under the combined action of centrifugal force and air jet force, the gripped filaments enter the conveying channel from the entrances on the bottom plate, and eventually are transported by the airflow into the collection bin.

2.3. Gripping Force Calculation

The essence of the gripping force is the frictional force between the rotating dual rollers and the filaments, which is closely related to the normal contact force between them. In this paper, the three-dimensional mechanism model is constructed based on the actual structure of the harvesting component, and the DEM numerical calculations are carried out to analyze the influence of structure and operating parameters on the gripping force [41–43]. The moisture content of filaments during the blooming period is high. When the filaments are squeezed, they undergo plastic deformation and simultaneously form adhesive contact with the surfaces of the dual rollers. The Hertz–Mindlin with JKR model considers adhesion governed by the interfacial surface energy; however, its normal contact law is still based on elastic contact and cannot describe loading-history-dependent plastic deformation. In contrast, the Edinburgh elasto-plastic adhesion (EEPA) model can describe the adhesive force associated with the plastic contact deformation of the filaments through its hysteretic elasto-plastic loading–unloading behavior and is therefore adopted for the filament–roller contact calculations [44].

As shown in Figure 3, the total normal contact force f_n can be expressed as the sum of the hysteretic spring force f_{hys} and the normal damping force f_{nd}. In Equations (1)–(3), compressive forces are taken as positive and attractive forces as negative.

$$f_n = f_{hys} + f_{nd} \tag{1}$$

where the f_{hys} and f_{nd} can be calculated by

$$f_{hys} = \begin{cases} f_0 + k_1\delta^n & \text{if } k_2(\delta^n - \delta_p^n) \geq k_1\delta^n \\ f_0 + k_2(\delta^n - \delta_p^n) & \text{if } k_1\delta^n > k_2(\delta^n - \delta_p^n) > -k_{adh}\delta^x \\ f_0 - k_{adh}\delta^x & \text{if } -k_{adh}\delta^x \geq k_2(\delta^n - \delta_p^n) \end{cases} \tag{2}$$

$$f_{nd} = -2\sqrt{\frac{5}{6}}\beta\sqrt{K_n m^*}v_n^{rel} \tag{3}$$

where δ is the contact overlap, δ_p is the residual plastic overlap, f_0 is the constant pull-off force, k_1 is the initial loading stiffness, k_2 is the unloading/reloading stiffness, k_{adh} is the adhesive stiffness, n is the power value for k_1 and k_2, x is the power value for k_{adh}, v_n^{rel} is the normal component of the relative velocity, β is the dimensionless damping coefficient, K_n is the normal contact stiffness used in the damping calculation, and m^* is the equivalent mass of the contacting bodies. Coetzee and Scheffler [44] provide detailed parameter definitions and calculation methods for the model. The contact forces were calculated using the built-in EEPA model in EDEM 2022.0, without modification of its contact-law implementation. The hysteretic spring force f_{hys} can be either compressive or attractive, depending on the contact state. When the contact is in an attractive state, the magnitude of this force is expressed as $|f_{hys}|$.

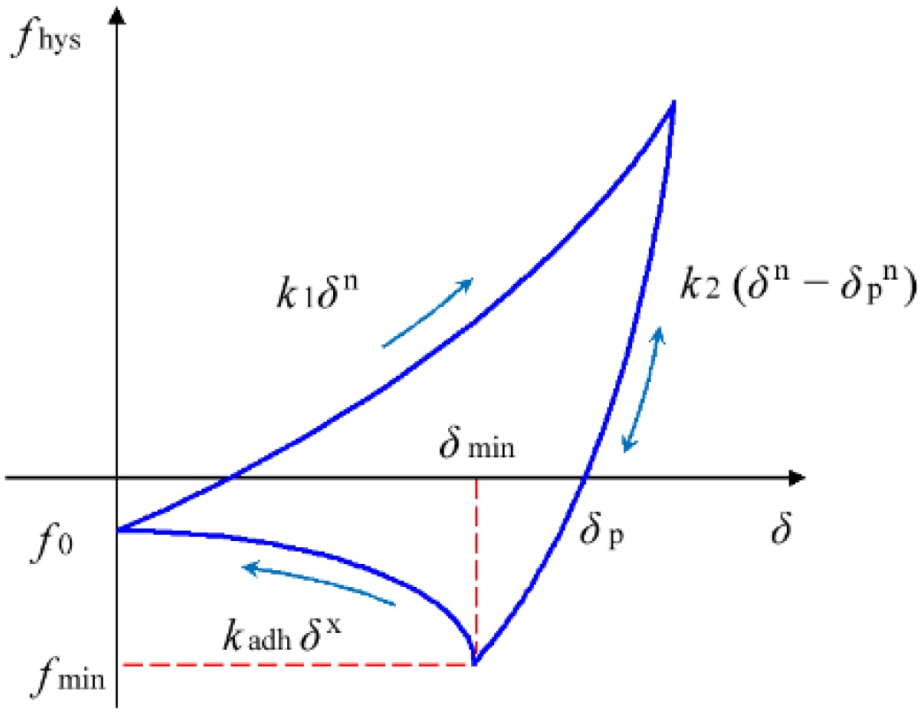


Figure 3. Schematic of contact force-displacement relationship in EEPA model.

To describe the bending and deformation properties of the flexible filaments, the meta-particle method is employed. Each filament is composed of 150 spherical elements with a radius of 0.20 mm, and the spherical elements are connected by bonding keys. The normal and tangential stiffnesses per unit area are 1.0×10^9 N/m^3 and 3.0×10^8 N/m^3, respectively. The critical normal and shear stresses are 5.0×10^7 Pa, and the bond disk radius is set to 0.24 mm. The coefficients used in the filament–roller contact calculation are $f_0 = -1.5 \times 10^{-4}$ N, $\Delta\gamma = 0.6$ J/m^2, $\lambda_p = 0.7$, $n = 1.5$, $x = 1.2$ and $\zeta_m = 0.8$. The density, Poisson's ratio and shear modulus of the polyurethane rollers were taken from the material specifications for the polyurethane used in the rollers and were kept constant during calibration. The filament–roller contact parameters were determined by comparing the macroscopic pulling and adhesion behaviors observed in the preliminary roller tests with those reproduced in the DEM simulations. During calibration, particular attention was paid to whether the filament bundle could be continuously drawn through the roller gap and whether residual adhesion occurred after the filaments left the minimum-gap region. The parameter combination given above reproduced both the pulling of the filaments at a roller gap of approximately 0.8 mm and their tendency to remain attached to the roller surfaces in the absence of the auxiliary air jets. It was therefore adopted in the subsequent simulations.

The calibrated model was subsequently used to compare the relative variations in the filament–roller contact forces and to determine the appropriate operating range under the investigated conditions.

The density, Poisson's ratio, shear modulus and filament–filament contact parameters were adopted from Zhang et al. [39]. The Poisson's ratio and shear modulus were obtained from compression tests on the floral necking region of a different safflower cultivar and were used here as approximate material inputs for the filament model. Their transfer to individual filaments was treated as a modeling assumption, since these properties were not independently determined for the material used in the present study. The density, Poisson's ratio and shear modulus of the polyurethane rollers were prescribed as model inputs, as listed in Table 1, and kept constant during calibration. The bond stiffnesses, critical stresses and bond radius were specified for the present meta-particle geometry using the parameter ranges investigated by Zhang et al. [39] as a reference. These values were model-specific inputs rather than direct adoption of the optimized bonding parameters reported in that study. The coefficients of restitution, static friction and rolling friction between the filaments and polyurethane rollers, together with the EEPA contact parameters, were determined through phenomenological calibration based on the observed macroscopic pulling behavior. During calibration, the related parameters were jointly and iteratively adjusted by comparing the filament feeding, compressive deformation, gripping and pulling, relative sliding, residual adhesion, adhesion-induced carry-back, and detachment behaviors obtained from the simulations with those observed in the physical dual-roller pulling tests, until the overall behaviors were in qualitative agreement. The value of n was fixed at 1.5 to retain a Hertzian-type nonlinear loading response, whereas the remaining filament–roller contact parameters were included in the joint calibration. The resulting parameter set was used to examine changes in filament–roller contact forces and the associated gripping condition. The predicted response to roller gap was compared with the field observations in Section 3.4. As the contact forces were not measured directly, the calculated force magnitudes and critical roller gap are treated as model-based estimates.

To examine the robustness of the derived gripping condition, a sensitivity analysis was performed using the force relationships given by Equations (8) and (9). The fitted coefficients f_0, a, and b for $f_{\mathrm{n,max}}$ and $f_{\mathrm{adh,max}}$, together with the filament–roller friction coefficient μ, were varied individually by $\pm 10\%$, while the remaining quantities were kept unchanged. At $\delta_c = 0.8$ mm and $\omega = 800$ rpm, the resulting values of $f_{\mathrm{n,max}}$, $f_{\mathrm{adh,max}}$, and F_{grip} ranged from 13.66 to 16.57 N, from 4.78 to 5.78 N, and from 12.85 to 15.70 N, respectively. The friction coefficient had the greatest direct influence on F_{grip}. Taking the upper limit of the measured filament separation force, 13.06 N, as the critical resistance, the calculated critical roller gap varied from 0.79 to 0.86 mm. Although the predicted force magnitudes changed, the transition between sufficient and insufficient gripping remained concentrated near a roller gap of 0.8 mm, supporting the stability of the selected operating range. The normal contact force f_{n} between the rollers and the filaments is variable, and its maximum value is related to the maximum contact overlap δ_{max}, which occurs at the position with the smallest dual-roller gap. According to Coulomb's law, as the normal contact force f_{n} acting on the filaments increases, the generated gripping force F_{grip} also increases. The critical condition for pulling out filaments from the flower bulb is that the gripping force F_{grip} should be greater than the separation force F_{s}. Otherwise, the filaments will remain on the flower bulb.

Critical gripping condition: $F_{\mathrm{grip}} > F_{\mathrm{s}}$.

2.4. Critical Condition for Filaments Separation

As the gripped filaments are transported toward the conveying chamber through the rotating dual rollers, they will be subjected to the adhesive forces and centrifugal forces. For the simplified separation analysis, the filaments are assumed to rotate with the roller immediately before detachment. In the reference frame rotating with the roller, the local outward normal is taken as the positive separation direction. The residual adhesive force acts toward the roller surface, whereas the centrifugal force F_c acts outward. The aerodynamic force F_a denotes the outward normal component of the airflow force on the filaments. Tangential friction does not enter this normal force balance, and gravity is neglected in the approximation. According to the characteristics of the EEPA contact model, the normal force corresponding to the maximum overlap δ_{max} can be expressed as

$$f_{hys,max} = f_0 + k_1\delta_{max}^n = f_0 + k_2\left(\delta_{max}^n - \delta_p^n\right) \tag{4}$$

The following can be obtained:

$$\delta_p^n = \frac{k_2 - k_1}{k_2}\delta_{max}^n \tag{5}$$

When the overlap unloaded to δ_{min}, there is

$$k_2{\delta_{min}}^n + k_{adh}{\delta_{min}}^x = k_2{\delta_p}^n \tag{6}$$

This indicates that as the maximum overlap δ_{max} increases, the normal contact force f_n increases, while the magnitude of the residual adhesive force f_{hys} also increases accordingly. The centrifugal force F_c is mainly related to the mass of the filaments m, rotational speed ω and radius of the roller R, which can be calculated as

$$F_c = m(\frac{2\pi\omega}{60})^2 R \tag{7}$$

In Equation (7), ω is the roller rotational speed in rpm, R is expressed in meters, and m is the mass of the filament or filament bundle considered in the separation analysis. All forces in the separation criterion refer to the same filament or filament bundle.

When the centrifugal force is insufficient to overcome the residual adhesion, the filaments may remain attached to the roller surfaces and rotate with them, resulting in the so-called "adhesion-induced carry-back" phenomenon. This requires applying additional auxiliary force F_a to assist the filaments separate from the dual-roller surfaces. The critical state of filament separation is reached when $F_a + F_c = |f_{hys}|$. Therefore, the condition for filament separation from the dual-roller surfaces can be expressed as

Critical separation condition: $F_a + F_c > |f_{hys}|$.

2.5. CFD–DEM Coupling Simulations

As analyzed previously, decreasing the dual-roller gap increases both the gripping force and the residual adhesive force. Therefore, successfully pulling the filaments and separating them from the dual rollers is a pair of contradictory objectives. The harvesting component retains the rubber strips used in the previous design [24] to remove filaments adhering to the roller surfaces. However, practical tests show that filament adhesion and carry-back remain evident with rubber-strip cleaning alone. Therefore, this paper introduces pneumatic-assisted separation, using two high-speed air jets to further assist the filaments in separating from the dual-roller surfaces. The air jets assist filament release without introducing an additional mechanical contact element.

To verify the dynamic process of filament separation from the dual-roller surfaces under airflow assistance, the CFD–DEM coupling simulation method [45] is adopted using ANSYS Fluent 2022 R1 and EDEM 2022.0. At the beginning of each simulation, 40 filaments are positioned 20 mm below the dual-roller gap and arranged in an inverted conical configuration to approximate their natural growth arrangement. The simulation represents the interaction of one filament bundle with one roller pair. The drive load of the harvesting component additionally depends on the number of flower bulbs engaged simultaneously across the three roller pairs.

The three-dimensional fluid domain of the harvesting component is extracted and discretized using an unstructured tetrahedral mesh comprising 1,716,510 cells and 307,755 nodes. The minimum orthogonal quality and maximum aspect ratio of the mesh are 0.06139 and 61.86, respectively. To assess the mesh sensitivity of the airflow prediction, coarse, medium and fine unstructured meshes containing approximately 0.90×10^6, 1.72×10^6 and 3.40×10^6 cells, respectively, were compared under the same computational conditions. The pressure difference ΔP, roller speed and conveying-fan pressure were maintained at 1.0 kPa, 800 rpm and 45 Pa, respectively. The local airflow velocity was evaluated at the measurement position described in Section 3.2, located 5 mm downstream of the air-slit outlet. The velocities obtained using the three meshes were 9.45, 9.91 and 9.98 m/s, respectively. Using the finer-mesh result in each comparison as the reference, the relative differences were 4.64% between the coarse and medium meshes and 0.70% between the medium and fine meshes. The latter was below the adopted criterion of 3%, and the mesh comprising 1,716,510 cells was therefore used for the subsequent CFD–DEM simulations.

A three-dimensional transient pressure-based solver with the absolute velocity formulation is used for the airflow calculations. The realizable k–ε turbulence model is adopted to characterize the jet flow issuing from the rectangular air outlets, and standard wall functions are used for near-wall treatment. The airflow field includes free-jet spreading, strong streamline curvature and local recirculation. Therefore, the realizable k–ε model is selected because it was developed and validated for planar and round jets, rotating shear flows and separated flows [46], while the standard wall functions are based on the classical near-wall treatment of Launder and Spalding [47]. The SIMPLE algorithm is used for pressure–velocity coupling, and the distance-based Rhie–Chow scheme is used for the flux calculation. Gradients are calculated using the least-squares cell-based method. The second-order scheme is used for pressure discretization, while the second-order upwind scheme is used for the momentum equations. The first-order upwind scheme is used for both the turbulent kinetic energy and turbulent dissipation rate equations. Time discretization is performed using the first-order implicit scheme. The absolute residual convergence criteria for continuity, the three velocity components, turbulent kinetic energy and turbulent dissipation rate are all set to 10^{-3}. A maximum of 20 iterations is allowed per CFD time step. Gravity is included with an acceleration of 9.81 m/s^2 in the positive y-direction. The constant pressure boundary and the non-slip wall conditions are used. The pressure at the conveying-fan outlet is 45 Pa. The airflow distributions and filament trajectories presented in the subsequent simulations are compared at total gauge pressures ΔP of 0, 0.5 and 1.0 kPa at the rectangular air-slit outlets.

Two-way CFD–DEM coupling was implemented using the EDEM–Fluent coupling interface. At each CFD time step, the positions, velocities and volumes of the spherical elements constituting the filaments were transferred from EDEM to Fluent to update the local solid volume fraction and particle-induced momentum source, while the aerodynamic forces calculated from the local airflow field were transferred back to EDEM to update the filament motion. The aerodynamic drag acting on each constituent sphere was calculated using the spherical drag law based on the Morsi–Alexander correlation. The CFD and

EDEM time steps were set to 1×10^{-3} s and 2×10^{-6} s, respectively. The selected EDEM time step corresponded to approximately 10.3% of the Rayleigh time calculated by EDEM. Within each CFD time step, EDEM was advanced by 500 substeps, and the physical times of the two solvers were synchronized during each data exchange. At a dual-roller rotational speed of 800 rpm, the selected CFD time step provided 75 airflow–particle coupling updates during each roller revolution.

3. Results and Discussion

3.1. Variation in Gripping Force

Figure 4 shows the variations in the normal contact force f_n when the dual-roller gap δ_c is 0.8 mm, the rotational speed ω is 800 and 1000 rpm, and the length of filaments L is 15 and 20 mm.

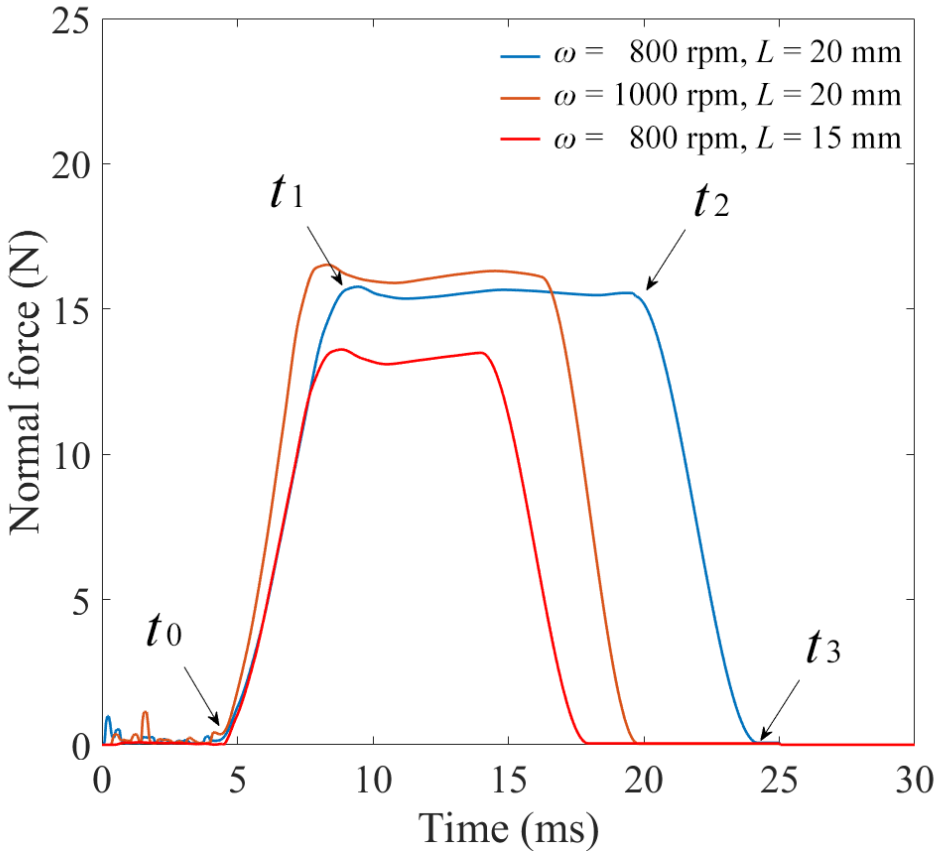


Figure 4. Variations in normal contact force.

At time t_0, the filaments begin to make contact with the dual-roller surfaces and are compressed as they enter the gap, causing the normal contact force f_n to increase rapidly. At time t_1, the force reaches its maximum value $f_{n,max}$ and remains close to this value until time t_2. Under the simulated conditions, the duration of this near-maximum-force stage increases with filament length L and decreases with roller speed ω. After time t_2, the filaments begin to leave the gap, and the normal contact force gradually decreases to approximately zero at time t_3. For L = 20 mm, increasing ω from 800 to 1000 rpm increases $f_{n,max}$ from approximately 16 to 16.5 N and shortens the near-maximum-force stage from approximately 12 to 9 ms. At ω = 800 rpm, decreasing L from 20 to 15 mm reduces $f_{n,max}$ from approximately 16 to 13.5 N and shortens this stage from approximately 12 to 7 ms.

To quantitatively analyze the influence of dual-roller gap δ_c on the maximum normal contact force, DEM simulations are carried out with the dual rollers' rotational speed ω of

800 rpm and δ_c varied within the range of 0.5–1.5 mm. Variations in the maximum normal contact force $f_{n,max}$ and the corresponding adhesive force $f_{adh,max}$ are shown in Figure 5.

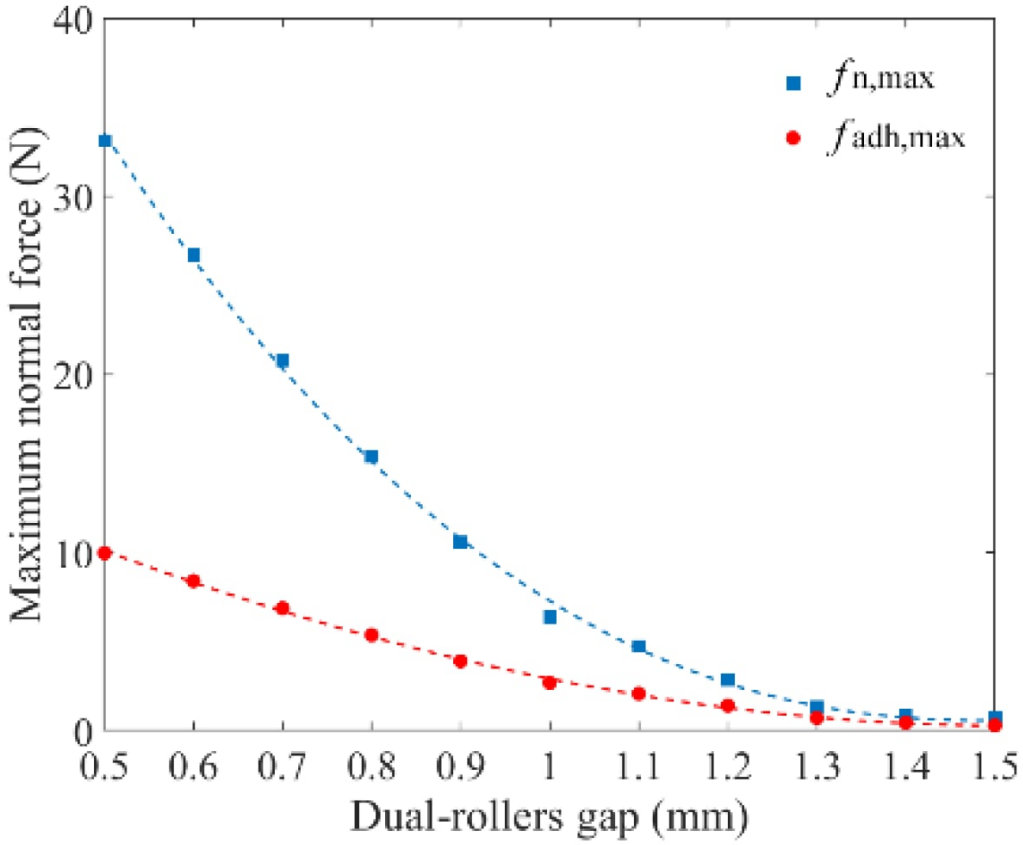


Figure 5. Variations in the maximum normal contact force and the corresponding adhesive force under different dual-roller gaps.

For each roller-gap condition in Figure 5, the normal and adhesive force results were obtained from the same simulation and refer to the same filament assembly. It can be seen that the dual-roller gap δ_c is the most important factor affecting the maximum normal contact force $f_{n,max}$ and the adhesive force $f_{adh,max}$. As δ_c decreases, both $f_{n,max}$ and $f_{adh,max}$ increase according to a power law relationship and can be fitted using the equation

$$f(\delta_c) = f_0 + a(1.5 - \delta_c)^b \quad (8)$$

where f_0 is the fitted force offset at δ_c = 1.5 mm and is distinct from the constant pull-off force denoted by the same symbol in Equation (2). The coefficients a and b are the proportional coefficient and the dimensionless exponent, respectively. The roller gap δ_c is entered in millimeters, and the fitted force is obtained in newtons. Based on the DEM simulation results, the following coefficients are obtained through nonlinear regression: the equation for $f_{n,max}$, f_0 = 0.575, a = 32.9, and b = 2.29; the equation for $f_{adh,max}$, f_0 = 0.297, a = 9.81, and b = 1.90. The coefficients of determination R^2 are greater than 0.998. According to the fitted relationships, when δ_c =0.8 mm, $f_{n,max}$ and $f_{adh,max}$ are approximately 15.11 and 5.28 N, respectively. With a filament–roller friction coefficient of 0.70, the corresponding gripping force is approximately 14.27 N, which is slightly greater than the upper limit of the measured filament separation force of 13.06 N. When the roller gap increases to 1.0 mm, $f_{n,max}$, $f_{adh,max}$ and F_{grip} decrease to approximately 7.30, 2.93 and 7.16 N, respectively, and the gripping force becomes lower than the measured separation-force range of 7.66–13.06 N.

These results explain why the pulling performance begins to deteriorate when the roller gap exceeds approximately 0.8 mm.

The robustness of this prediction was further examined by varying each fitted coefficient and the filament–roller friction coefficient individually by ±10%, while keeping the remaining quantities unchanged, as described in Section 2.3. At δ_c = 0.8 mm, the resulting ranges of $f_{n,max}$, $f_{adh,max}$ and F_{grip} were 13.66–16.57, 4.78–5.78 and 12.85–15.70 N, respectively. At δ_c = 0.7 mm, F_{grip} remained between 17.03 and 20.81 N and was consistently greater than the upper reported filament separation force of 13.06 N. By contrast, at δ_c = 0.9 mm, it decreased to 9.33–11.40 N and could no longer overcome the separation resistance of all filament bundles. Taking 13.06 N as the reference resistance, the calculated critical roller gap ranged from approximately 0.79 to 0.86 mm. The transition in the pulling condition therefore remained concentrated near a roller gap of 0.8 mm, although filament bundles with relatively high separation resistance may not be completely detached under the lower-bound condition.

The approximate 95% confidence intervals for f_0, a, and b are [−0.5981, 1.7494], [31.4258, 34.4655], and [2.0474, 2.5423], respectively, for $f_{n,max}$, and [−0.0811, 0.6744], [9.3452, 10.2816], and [1.6930, 2.1122], respectively, for $f_{adh,max}$. The RMSEs between the fitted and DEM-calculated forces were 0.4308 and 0.1303 N for the maximum normal contact force and adhesive force, respectively, and the corresponding MAEs were 0.3721 and 0.1153 N.

The forces acting on the filaments during gripping by the dual rollers are shown in Figure 6.

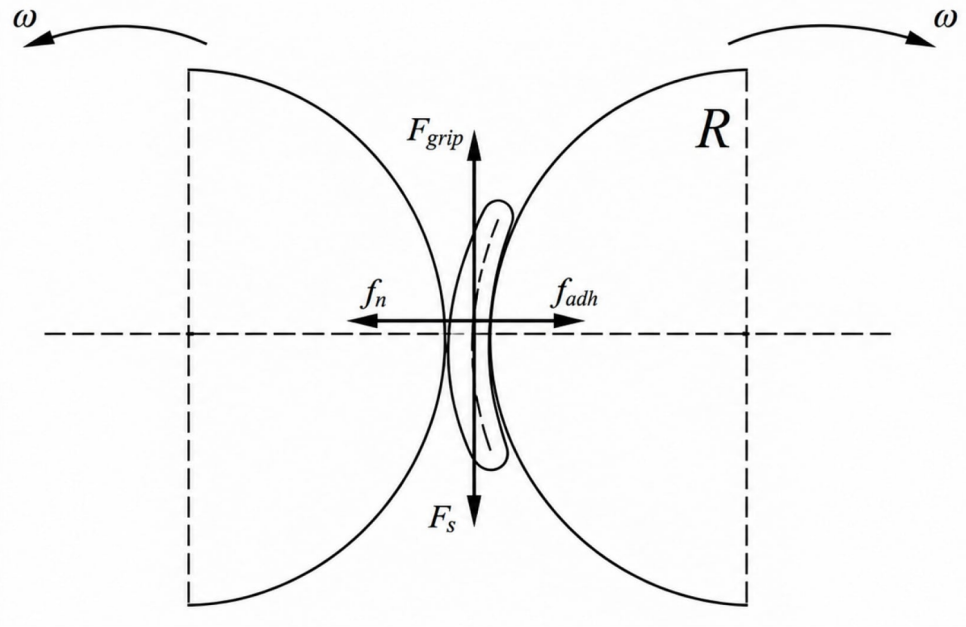


Figure 6. Free-body diagram of the filaments during dual-roller gripping.

The gripping force acting on filaments can be expressed as

$$F_{grip} = \mu(f_n + f_{adh}) \tag{9}$$

Because the friction coefficient μ between the filaments and the roller surface is about 0.7, and the separation force F_s between the filaments and the flower bulb ranges from 7.66 to 13.06 N, the filaments can be effectively gripped when δ_c is less than 0.8 mm. This criterion describes the force required for filament detachment; the load limits for filament and plant damage were not determined in this study. At δ_c = 0.8 mm, the fitted maximum

adhesive force magnitude is approximately 5.28 N and increases as the roller gap decreases. This increased adhesion can promote filament carry-back when the outward separation forces are insufficient.

Each motor drives the three roller pairs of one harvesting component. Observations during harvesting showed that one or two capitula were typically engaged simultaneously across these three roller pairs. Taking the upper reported filament detachment force of 13.06 N per flower bulb [38] as a reference, the combined equivalent resisting torque at the rollers is estimated to be 0.196–0.392 N·m for a roller radius of 15 mm. At 800 rpm, the corresponding mechanical power for filament pulling is approximately 16.4–32.8 W. With a roller-to-motor speed ratio of 1.2, the corresponding motor-shaft torque is 0.235–0.470 N·m. This simplified estimate assumes that the engaged capitula reach the reference detachment force simultaneously and neglects transmission losses and other mechanical resistance. For the observed simultaneous engagement of one or two capitula, the estimated motor-shaft torque is below the specified rated torque of 0.637 N·m under these assumptions.

3.2. Variation in Airflow Field

When positive pressure is applied to the rectangular air outlets on two sides of the dual rollers, two jets will be formed in the filament entrance channel. To analyze the influence of pressure difference ΔP on the airflow distribution, CFD simulations are carried out at ΔP = 0, 0.5 and 1.0 kPa, as shown in Figure 7.

When ΔP = 0, due to the influence of the self-rotation of the dual rollers, ω = 800 rpm, there is an airflow disturbance layer near the roller surfaces. The airflow velocity is approximately 1.4 m/s, which is slightly greater than the peripheral speed of the rollers. The inner cavity of the conveying channel is a stable airflow field established by the conveying fan. The airflow velocity is related to the pressure difference in the conveying fan and is approximately 4.8 m/s, exceeding the suspension velocity range of 1.59–2.91 m/s reported by Ge et al. [38]. When ΔP = 0.5 kPa is applied, the air jet velocity v_{gap} at the gaps between the dual-rolls and the bottom plate is approximately 6–8 m/s, and the directions are tangent to the corresponding dual-rolls surfaces. These jets exert aerodynamic forces on the filaments, thereby helping them separate from the dual-roller surfaces. When the left air jet enters the conveying channel, its interaction with the conveying airflow forms a local low-speed recirculation zone, which may alter the trajectories of filaments entering the chamber. An additional airflow with a velocity of approximately 2.7 m/s develops below the dual-roller gap and may affect filament entry into the gap. When ΔP is further increased to 1.0 kPa, the overall distribution of the airflow field does not change significantly. The major difference is that the air jet velocity v_{gap} is increased to 10.0 m/s, and the filament separation performance can be further enhanced.

At a pressure difference of 1.0 kPa and a roller speed of 800 rpm, the airflow velocity was measured using a JT1432 omnidirectional thermal air velocity sensor (Beijing Century Jiantong Technology Co., Ltd., Beijing, China), with its sensing element positioned 5 mm downstream of the air-slit outlet. The conveying-fan pressure was maintained at 45 Pa. Five repeated measurements gave an airflow velocity of 9.60 ± 0.13 m/s (mean ± standard deviation, n = 5). The local velocity predicted using the adopted medium mesh at the same position was 9.91 m/s, as reported in Section 2.5. The predicted and measured velocities were compared using the same velocity definition and averaging procedure. The difference between the predicted and measured mean velocities was approximately 0.31 m/s, corresponding to a relative difference of approximately 3.2%. The sensor's specified accuracy was ± (0.2 m/s + 2% of the reading), corresponding to approximately ±0.39 m/s at the measured velocity. This comparison supports the local airflow prediction at the tested position and operating condition.

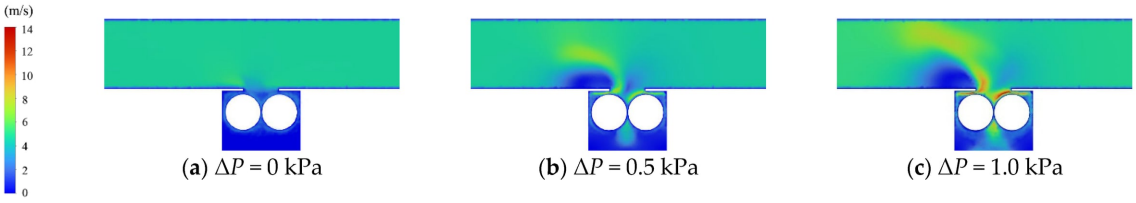


Figure 7. Variations in airflow field distribution.

3.3. Dynamics of Filament Separation

In this section, to obtain the motion trajectory of the filaments and determine the reasonable range of positive pressure difference, the CFD–DEM coupling method is used to simulate the dynamic gripping process of filaments assisted by the jet airflows. The filament motion states with a dual-roller gap δ_c of 0.8 mm and pressure differences ΔP of 0, 0.5 and 1.0 kPa are shown in Figure 8, in which the time axis is basically consistent with that of Figure 4.

When ΔP = 0, some filaments in the center of the cluster do not directly come into contact with the dual-roller surfaces. The adhesive forces acting on them are relatively small. After 20 ms, they can be ejected from the gap by centrifugal force and enter into the conveying chamber, and then be transported through the airflow field in the chamber. However, 30 out of the 40 filaments in contact with the dual-roller surfaces are adhered and rotate along with rollers because the adhesive forces acting on them are greater than the centrifugal forces, as shown in Figure 8c. When ΔP = 0.5 kPa is applied, under the action of the air jets, the number of filaments adhering to the roller surfaces decreases from 30 to 12, as shown in Figure 8f. The filaments that separate from the gap rapidly disperse along the direction of the airflow shown in Figure 7, and then enter the conveying chamber. When ΔP increases to 1.0 kPa, the filaments move away from the roller surfaces and enter the conveying chamber, as shown at 30 ms in Figure 8i.

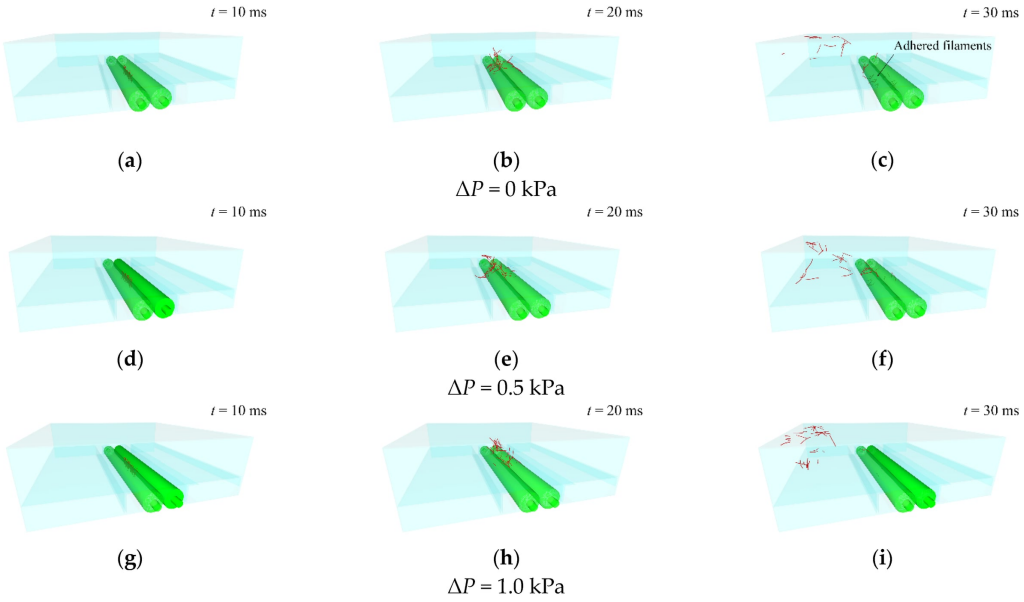


Figure 8. CFD–DEM coupling simulations of filament movement at a dual-roller gap of 0.8 mm and a roller speed of 800 rpm: (**a**–**c**) ΔP = 0 kPa; (**d**–**f**) ΔP = 0.5 kPa; (**g**–**i**) ΔP = 1.0 kPa. The three columns show the filament configurations at 10, 20 and 30 ms, respectively.The red lines in the figure represent safflower filaments.

Figure 9 shows the normal contact force on the dual rollers over a 200 ms interval. At a roller speed of 800 rpm, one revolution takes approximately 75 ms. The initial gripping stage produces the main force peak under all three pressure conditions. At ΔP = 0 and 0.5 kPa, smaller force peaks recur during subsequent roller revolutions, consistent with retained filaments being carried back toward the gap and compressed again. At ΔP = 1.0 kPa, the normal contact force decreases to approximately zero after 20 ms, and no distinct renewed compression peak appears during the remaining observation period. Together with the filament configuration at 30 ms in Figure 8i, this response indicates reduced adhesion-induced carry-back.

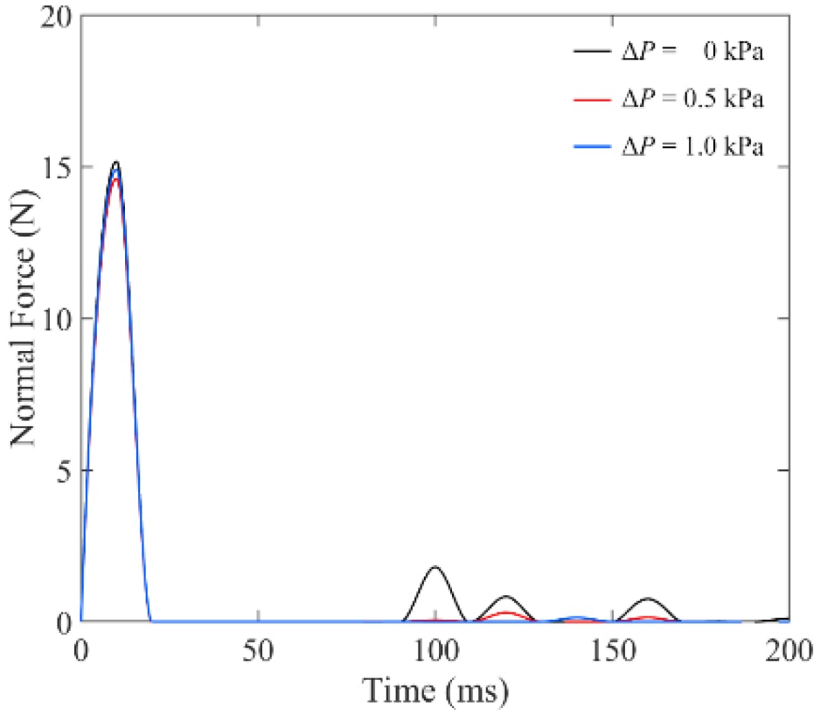


Figure 9. Force variations on dual rollers during multiple rotation cycles.

Based on the gripping-force analysis and the simulated filament trajectories, a dual-roller gap δ_c of 0.8 mm, a roller speed ω of 800 rpm and a pressure difference ΔP of 1.0 kPa are selected for field evaluation. Under this condition, the simulations show filament release from the roller surfaces and reduced carry-back during the subsequent roller revolutions.

3.4. Machine Development and Field Tests

A fresh safflower filaments harvesting machine is developed, as shown in Figure 10a. The machine has overall dimensions of 1500 × 1000 × 1600 mm, and its operating mass under full-load conditions is approximately 350 kg. The chassis movement is powered by four hub motors with a torque of 150 N·m, and the machine achieves differential movement by coordinating the control of the speeds of the motors. Six sets of harvesting components are installed on the frame in a 2 × 3 configuration, enabling the machine to harvest two rows of safflower filaments simultaneously. Each harvesting component can move linearly in the vertical direction under the drive of an independent electric cylinder. Two channels for safflower plants are added in the middle of the frame. There are active supporting claws in the channel, whose linear velocity is consistent with the machine's forward speed, but in the opposite direction. As the machine moves forward, the safflower plants enter the channel. The supporting claws can stabilize the plant stems to reduce swaying. Infrared gratings are installed below each harvesting component to detect the height position of the filaments. The hub motors, roller-driving motors, electric cylinders, conveyor fans, and

control system are powered by 24 V batteries, with an estimated rated power demand of approximately 7.0 kW. Positive pressure airflow is provided using a 5.0 kW high-pressure turbine fan independently powered by a 220 V gasoline generator, and the gauge pressure at the fan outlet can be adjusted within the range of 0 to 5.0 kPa. Therefore, the total installed electrical power demand of the machine under rated-load conditions is estimated to be approximately 12.0 kW.

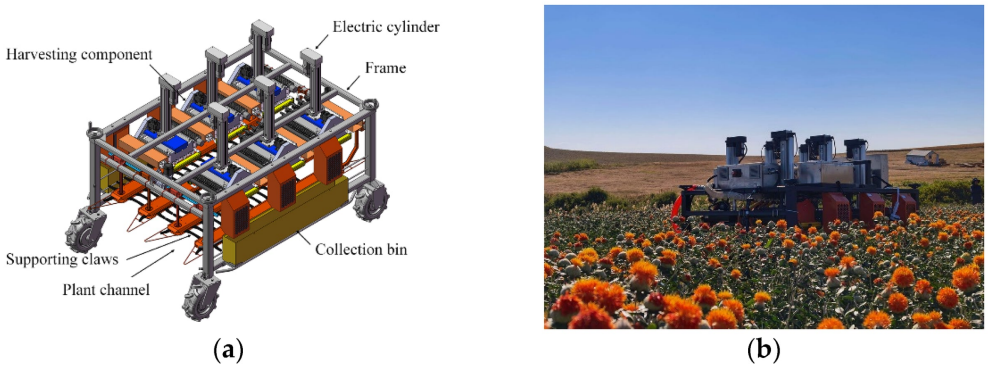


Figure 10. Harvester structure and field harvesting of safflower filaments. (**a**) Overall schematic of the machine; (**b**) field tests

The harvesting experiments were carried out in Yumin county, Xinjiang Uyghur autonomous region (82.64° E, 46.03° N) in July 2025, as shown in Figure 10b. These tests formed part of the same field experimental campaign as that reported by Wang et al. [24], using the jointly developed harvesting platform. The safflower variety used in the field tests is 'Yumin Wuci', and the plants were at the full flowering stage. The average moisture content of the filaments was 68.5%. During the field tests, the forward speed of the machine was set to 0.15 m s^{-1}. Based on the two-row working width of 0.8 m, the theoretical harvesting capacity was approximately 0.0432 ha h^{-1}. A one-factor-at-a-time arrangement was used, with δ_c = 0.8 mm, ω = 800 rpm and ΔP = 1.0 kPa as the reference operating condition. The roller gap was set to 0.6, 0.8 and 1.0 mm, the roller speed to 600, 800 and 1000 rpm, and the pressure difference to 0 and 1.0 kPa. For each comparison, the other two operating parameters were maintained at their reference values. The common reference condition was counted only once, giving six operating conditions, as summarized in Table 2. The rubber-strip cleaning structure was retained in both airflow conditions to examine the additional effect of pneumatic-assisted separation. The field measurements reported in Table 2, including those from the roller gap, roller speed and airflow comparisons, were not used in Wang et al. [24].

Table 2. Field harvesting performance under different operating conditions.

δ_c (mm)	ω (rpm)	ΔP (kPa)	Pulling-Out Rate η_p (%)	Loss Rate η_l (%)	Effective Collection Rate η (%)
0.6	800	1.0	92.0 ± 0.8	8.5 ± 0.6	83.5 ± 0.2
0.8	800	1.0	91.4 ± 0.6	7.1 ± 0.4	84.3 ± 0.2
1.0	800	1.0	55.0 ± 2.5	4.0 ± 0.5	51.0 ± 2.0
0.8	600	1.0	90.8 ± 0.7	7.6 ± 0.4	83.2 ± 0.3
0.8	1000	1.0	91.1 ± 0.8	6.6 ± 0.2	84.5 ± 0.6
0.8	800	0	90.9 ± 1.1	40.2 ± 1.6	50.7 ± 2.7

Values are means ± standard deviations of three spatially separated sampling sections within one field pass for each operating condition (n = 3). The standard deviations describe within-pass spatial variation, not variability among independent passes.

Each operating condition was evaluated in one 15 m field pass. After the machine reached stable operation, three spatially separated, non-overlapping 1-m-long sampling sections were selected within the pass. The three performance indices were calculated separately for each section, and their means and standard deviations were then calculated across the three sections. Thus, n = 3 represents spatial subsamples within a single pass rather than independent experimental passes. Comparisons among operating conditions were therefore descriptive.

To describe the quality of harvesting operations, three performance indices are defined: the filament pulling-out rate η_{p}, the loss rate η_{l} and the effective collection rate η. These indices are calculated using the same denominator:

$$\eta_p = \frac{m_p}{m_t} \times 100\% \tag{10}$$

$$\eta_l = \frac{m_p - m_c}{m_t} \times 100\% \tag{11}$$

$$\eta = \frac{m_c}{m_t} \times 100\% = \eta_p - \eta_l \tag{12}$$

where m_{t} is the estimated harvestable filament mass before harvesting, m_{p} is the filament mass pulled from the capitula, and m_{c} is the collected filament mass for the same sampling section. All masses are expressed in grams. The mass m_{p} was obtained by direct weighing, and m_{c} was determined separately for each 1 m sampling section. The harvestable filament mass per unit area was determined by sampling and weighing the reference sections. For each harvesting sampling section, m_{t} was estimated by multiplying its area by the mean harvestable filament mass per unit area across the reference sections.

This estimate assumes that the reference sections are representative of the harvested sampling sections. The harvestable filament mass per unit area in the reference sections differed from their mean by up to 15%, indicating spatial variation in the available filament mass. Since m_{p} and m_{c} were measured independently of m_{t}, all three calculated indices vary inversely with the reference-mass estimate. The reported standard deviations describe variation among the three section-level indices within each pass; they do not quantify the uncertainty of the reference-mass estimate. Small differences among operating conditions should therefore be interpreted cautiously.

At ω = 800 rpm and ΔP = 1.0 kPa, decreasing δ_{c} from 0.8 to 0.6 mm increased the pulling-out rate η_{p} only slightly, from 91.4 $\pm$ 0.6% to 92.0 $\pm$ 0.8%. However, the loss rate η_{l} increased from 7.1 $\pm$ 0.4% to 8.5 $\pm$ 0.6%, and the effective collection rate η consequently decreased from 84.3 $\pm$ 0.2% to 83.5 $\pm$ 0.2%. When δ_{c} increased to 1.0 mm, η_{p} decreased to 55.0 $\pm$ 2.5%, while η decreased to 51.0 $\pm$ 2.0%. According to Equations (8) and (9), the predicted gripping force is approximately 14.27 N at δ_c =0.8 mm, which is slightly greater than the upper limit of the measured filament separation force of 13.06 N. When δ_c increases to 1.0 mm, the predicted gripping force decreases to approximately 7.16 N, which is lower than the measured separation-force range of 7.66–13.06 N. The predicted decrease in gripping force as the roller gap increased from 0.8 to 1.0 mm is consistent with the reduction in the field pulling-out rate. This agreement supports the predicted trend with roller gap under the tested conditions. Relatively small capitula could enter the harvesting-component entrances under this condition, but their filaments were not effectively pulled out. At δ_{c} =0.8 mm and ΔP = 1.0 kPa, changing ω from 600 to 1000 rpm resulted in pulling-out rates of 90.8 $\pm$ 0.7%, 91.4 $\pm$ 0.6% and 91.1 $\pm$ 0.8%, respectively, while the corresponding effective collection rates were 83.2 $\pm$ 0.3%, 84.3 $\pm$ 0.2% and 84.5 $\pm$ 0.6%. The measured responses changed only slightly with rotational speed within the tested range. These differences, together with the small difference in effective collection rate

between roller gaps of 0.6 and 0.8 mm, do not provide sufficient evidence to establish a unique optimum within the tested settings.

During field harvesting operations, the successful pulling of filaments from the capitula is not only dependent on the gripping force F_{grip}, but may also be influenced by capitulum orientation, height distribution, and maturity. These morphological factors may affect whether the capitula can smoothly enter the filament entrances of the harvesting components and then be gripped by the rotating dual rollers. However, these morphological variables were not recorded for individual capitula in the present field tests; therefore, their effects could not be statistically separated from those of the machine operating parameters.

At δ_c = 0.8 mm and ω = 800 rpm, the pulling-out rate was 90.9 ± 1.1% when ΔP = 0. However, a large amount of the pulled-out filaments was carried back by the dual rollers and subsequently fell onto the field or the machine frame, as shown in Figure 11c. The resulting loss rate was 40.2 ± 1.6%, and the effective collection rate was 50.7 ± 2.7%. When ΔP = 1.0 kPa was applied, the pulling-out rate changed only slightly to 91.4 ± 0.6%, whereas the loss rate decreased to 7.1 ± 0.4% and the effective collection rate increased to 84.3 ± 0.2%. Thus, increasing ΔP from 0 to 1.0 kPa reduced the loss rate by 33.1 percentage points and increased the effective collection rate by 33.6 percentage points. Under the tested conditions, the airflow comparison showed a much larger difference in effective collection rate than in pulling-out rate, consistent with the observed reduction in adhesion-induced carry-back. The collected filaments appeared largely intact on visual inspection, as shown in Figure 11d.



Figure 11. Field harvesting performance test results. The photographs in panels (**a**,**b**) show the same field experimental campaign reported by Wang et al. [24]. (**c**) Harvesting channel; (**d**) Comparison of manual and mechanical harvesting of safflower filaments (mechanical harvesting on the left).

For the jointly developed dual-roller harvesting system, Wang et al. [24] investigated plant feeding and coordinated canopy coverage. The present study focuses on filament release after pulling. The field tests show that filament carry-back persists with rubber-strip cleaning alone, whereas the addition of pneumatic assistance improves filament release and collection. These results indicate that effective harvesting requires both sufficient gripping to pull the filaments and reliable release from the roller surfaces.

4. Conclusions

In this paper, the harvesting method using dual-roller gripping and pneumatic-assisted separation is proposed and a harvesting machine for fresh safflower filaments is developed.

A flexible model of the filament is established, and the viscous contact mechanical properties between the filaments and the dual rollers are calculated using the EEPA model. The dynamic process of filament harvesting is analyzed using CFD–DEM coupling simulations. Within the simulated dual-roller gap range of 0.5–1.5 mm, the maximum normal contact force and adhesive force increase with decreasing gap according to power law relationships, with coefficients of determination R^2 greater than 0.998. In the field tests, at ω = 800 rpm and ΔP = 1.0 kPa, dual-roller gaps of 0.6 and 0.8 mm produced pulling-out rates of 92.0 $\pm$ 0.8% and 91.4 $\pm$ 0.6%, respectively, whereas increasing the gap to 1.0 mm reduced the pulling-out rate to 55.0 $\pm$ 2.5%. At δ_c = 0.8 mm and ω = 800 rpm, increasing ΔP from 0 to 1.0 kPa reduced the loss rate from 40.2 $\pm$ 1.6% to 7.1 $\pm$ 0.4% and increased the effective collection rate from 50.7 $\pm$ 2.7% to 84.3 $\pm$ 0.2%. Changing the rotational speed from 600 to 1000 rpm produced only limited variation in the pulling-out and effective collection rates under the tested conditions. These results indicate that the positive air jets mainly improve effective collection by reducing adhesion-induced carry-back. The reported standard deviations describe spatial variation among three sampling sections within one experimental pass and do not represent repeatability between independent passes. Therefore, the field results should be interpreted within the tested operating ranges, crop conditions and single-pass experimental arrangement, with additional uncertainty arising from the reference harvestable-mass estimate.

Author Contributions: Conceptualization, Y.G. and Y.Z.; methodology, Z.Z. and Z.X.; software, Z.W.; validation, Z.X.; investigation, Q.Z.; resources, Y.G. and Y.Z.; data curation, Q.Z.; writing—original draft preparation, Z.W.; writing—review and editing, Z.Z.; supervision, Z.Z. All authors have read and agreed to the published version of the manuscript.

Funding: This research was funded by the National Natural Science Foundation of China (grant numbers 52375247 and 32260430) and the Priority Academic Program Development of Jiangsu Higher Education Institutions (grant number PAPD-2023-87).

Data Availability Statement: The raw data supporting the conclusions of this article will be made available by the authors on request.

Conflicts of Interest: The authors declare that they have no known competing financial interests or personal relationships that could have appeared to influence the work reported in this paper. Author Zhen Xue was employed by the company Taizhou Xiechuang Agricultural Equipment Co., Ltd. The remaining authors declare that the research was conducted in the absence of any commercial or financial relationships that could be construed as a potential conflict of interest.

References

1. Patanè, C.; Cosentino, S.L.; Calcagno, S.; Pulvirenti, L.; Siracusa, L. How do sowing time and plant density affect the pigments safflomins and carthamin in florets of safflower? *Ind. Crops Prod.* **2020**, *148*, 112313. [CrossRef]
2. Zanetti, F.; Angelini, L.G.; Berzuini, S.; Foschi, L.; Clemente, C.; Ferioli, F.; Vecchi, A.; Rossi, A.; Monti, A.; Tavarini, S. Safflower (*Carthamus tinctorius* L.) a winter multipurpose oilseed crop for the Mediterranean region: Lesson learnt from on-farm trials. *Ind. Crops Prod.* **2022**, *184*, 115042. [CrossRef]
3. Delshad, E.; Yousefi, M.; Sasannezhad, P.; Rakhshandeh, H.; Ayati, Z. Medical uses of *Carthamus tinctorius* L. (Safflower): A comprehensive review from traditional medicine to modern medicine. *Electron. Physician* **2018**, *10*, 6672–6681. [CrossRef] [PubMed]
4. Kadirvel, P.; Veerraju, C.; Senthilvel, S.; Yadav, P.; Kiran, B.U.; Shaik, M.; Shaw, R.; Mani, S.V.; Reddy, Y.R.; Mohanrao, M.D.; et al. Marker-assisted selection for fast-track breeding of high oleic lines in safflower (*Carthamus tinctorious* L.). *Ind. Crops Prod.* **2020**, *158*, 112983. [CrossRef]
5. Mani, V.; Lee, S.-K.; Yeo, Y.; Hahn, B.-S. A metabolic perspective and opportunities in pharmacologically important safflower. *Metabolites* **2020**, *10*, 253. [CrossRef] [PubMed]

6. Li, J.; Wang, R.; Chen, C.; Huang, X.; Xian, B.; Lv, T.; Ren, C.; Wu, Q.; Wen, F.; Yan, J.; et al. Effects of drying processes on the chemical and physical properties of safflower: Towards a multidimensional quality evaluation model. *PLoS ONE* **2026**, *21*, e0339180. [CrossRef] [PubMed]
7. Torabi, B.; Adibnya, M.; Rahimi, A.; Azari, A. Modeling flowering response to temperature and photoperiod in safflower. *Ind. Crops Prod.* **2020**, *151*, 112474. [CrossRef]
8. Cheng, Y.; Wang, C.; Dong, G.; Li, X.; Huang, T.; Su, J. Detecting safflower at the full bloom stage using lightweight YOLO-GESCW. *Trans. Chin. Soc. Agric. Eng.* **2026**, *42*, 33–42. (In Chinese) [CrossRef]
9. Steberl, K.; Hartung, J.; Graeff-Hönninger, S. Impact of cultivar, harvest date and threshing parameter settings on floret and carthamidin yield of safflower. *Agronomy* **2020**, *10*, 1272. [CrossRef]
10. Azimi, S.; Chegini, G.; Kianmehr, M.H. Design and manufacture of safflower petal harvester machine. *Mech. Ind.* **2012**, *13*, 301–305. [CrossRef]
11. Zhang, Z.G.; Lv, Q.G.; Ren, J.Y.; Han, C.J.; Yuan, P.P.; Zhang, X.J. Design of critical components for safflower harvesting machinery by rotary shear. *J. Chin. Agric. Mech.* **2019**, *40*, 1–6. [CrossRef]
12. Zhang, Z.G.; Zhao, M.Y.; Xing, Z.Y.; Liu, X.F. Design and test of double-acting opposite direction cutting end effector for safflower harvester. *Trans. Chin. Soc. Agric. Mach.* **2022**, *53*, 160–170. [CrossRef]
13. Han, D.D.; Ge, Y.; Tang, M.J.; Li, Y.; Yi, J.J. Design of cutting-air suction safflower filament harvesting device. *J. Agric. Mech. Res.* **2014**, *36*, 120–123. [CrossRef]
14. Huang, Y.; Ge, Y.; Zhang, L.X.; Gu, J.W.; Qian, Y.; Liang, D.D. Dynamic model for sucking process of pneumatic-cutting type safflower harvest device. *J. Agric. Mech. Res.* **2016**, *38*, 41–45. [CrossRef]
15. Liu, G.X.; Ge, Y.; Zhang, L.X.; Zhao, Q.Z.; Zhang, T.Y. Design of cutting-safflower picking experiment platform and experimental study on picking performance. *Mach. Des. Res.* **2019**, *35*, 178–183. [CrossRef]
16. Chen, B.B.; Yao, Q.J.; Ding, F.; Li, K.; Ma, B.J. Design and optimization of a negative pressure rotary cutting safflower filaments harvesting device. *Sci. Rep.* **2025**, *15*, 9693. [CrossRef] [PubMed]
17. He, H.H.; Yang, S.P.; Feng, W. Design and test of guide rail pulling type safflower harvesting device. *J. Chin. Agric. Mech.* **2024**, *45*, 42–48. [CrossRef]
18. Yang, S.P.; Ye, Y.X.; Guo, G.; Zhang, Y. Design and test of flexible clamping device for safflower. *J. Chin. Agric. Mech.* **2025**, *46*, 14–19. [CrossRef]
19. Du, C.; Fang, W.; Han, D.; Chen, X.; Wang, X. Design and experimental study of a biomimetic pod-pepper-picking drum based on multi-finger collaboration. *Agriculture* **2024**, *14*, 314. [CrossRef]
20. Han, D.; Zhang, H.; Li, G.; Wang, G.; Wang, X.; Chen, Y.; Chen, X.; Wen, X.; Yang, Q.; Zhao, R. Development of a bionic picking device for high harvest and low loss rate pod pepper harvesting and related working parameter optimization details. *Agriculture* **2024**, *14*, 859. [CrossRef]
21. Ge, Y.; Zhang, L.X.; Gu, J.W.; Fu, W.; Zhu, R.G.; Zhang, H.M. Parameter optimization and experiment of dual roller harvesting device for safflower. *Trans. Chin. Soc. Agric. Eng.* **2015**, *31*, 35–42. [CrossRef]
22. Zhang, T.Y.; Zhang, L.X.; Ge, Y.; Liu, G.X.; Zhang, X.W. Development and test of a portable roller-type safflower harvester. *J. Agric. Mech. Res.* **2020**, *42*, 76–81. [CrossRef]
23. Guo, H.; Luo, D.; Gao, G.; Wu, T.; Diao, H. Design and experiment of a safflower picking robot based on a parallel manipulator. *Eng. Agríc.* **2022**, *42*, e20210129. [CrossRef]
24. Wang, Z.X.; Zheng, Y.J.; Ge, Y.; Zeng, H.F.; Yuan, L.X. Design and experiment of the safflower picking equipment with parallel multi-picking heads. *Trans. Chin. Soc. Agric. Eng.* **2026**, *42*, 55–66. [CrossRef]
25. Xu, L.; Li, Y.; Chai, X.; Wang, G.; Liang, Z.; Li, Y.; Li, B. Numerical simulation of gas–solid two-phase flow to predict the cleaning performance of rice combine harvesters. *Biosyst. Eng.* **2020**, *190*, 11–24. [CrossRef]
26. Wang, S.; Shen, K.; Xiong, H.; Lin, J.; Guo, Y. A numerical investigation on segregation in gas-fluidized beds of short, flexible fibers. *Adv. Powder Technol.* **2024**, *35*, 104304. [CrossRef]
27. Ding, B.; Liang, Z.; Qi, Y.; Ye, Z.; Zhou, J. Improving cleaning performance of rice combine harvesters by DEM–CFD coupling technology. *Agriculture* **2022**, *12*, 1457. [CrossRef]
28. Liu, W.; Zeng, S.; Chen, X. Vortex cleaning device for rice harvester: Design and bench test. *Agriculture* **2024**, *14*, 866. [CrossRef]
29. Ou, M.; Wang, G.; Lu, Y.; Zhang, Z.; Pan, H.; Jia, W.; Dong, X. Structure optimization and performance simulation of a double-disc fertilizer spreader based on EDEM-CFD. *Agronomy* **2025**, *15*, 1025. [CrossRef]
30. Leblicq, T.; Smeets, B.; Vanmaercke, S.; Ramon, H.; Saeys, W. A discrete element approach for modelling bendable crop stems. *Comput. Electron. Agric.* **2016**, *124*, 141–149. [CrossRef]
31. Horabik, J.; Molenda, M. Parameters and contact models for DEM simulations of agricultural granular materials: A review. *Biosyst. Eng.* **2016**, *147*, 206–225. [CrossRef]
32. Xu, Y.; Zhang, X.; Wu, S.; Chen, C.; Wang, J.; Yuan, S.; Chen, B.; Li, P.; Xu, R. Numerical simulation of particle motion at cucumber straw grinding process based on EDEM. *Int. J. Agric. Biol. Eng.* **2020**, *13*, 227–235. [CrossRef]

33. Schramm, M.; Tekeste, M.Z. Wheat straw direct shear simulation using discrete element method of fibrous bonded model. *Biosyst. Eng.* **2022**, *213*, 1–12. [CrossRef]
34. Korn, C.; Herlitzius, T. Coupled CFD–DEM simulation of the separation process in combine harvester cleaning devices. *Landtechnik* **2017**, *72*, 247–262. [CrossRef]
35. Xu, P.; Dai, F.; Shi, R.; Zhang, S.; Zhao, Q.; Pan, H.; Qu, J. Design and optimization of air suction cleaning device for flaxseed based on NSGA-II algorithm and CFD-DEM simulation. *Ind. Crops Prod.* **2025**, *236*, 121866. [CrossRef]
36. Kieckhefen, P.; Pietsch, S.; Dosta, M.; Heinrich, S. Possibilities and Limits of Computational Fluid Dynamics–Discrete Element Method Simulations in Process Engineering: A Review of Recent Advancements and Future Trends. *Annu. Rev. Chem. Biomol. Eng.* **2020**, *11*, 397–422. [CrossRef] [PubMed]
37. Bräsel, B.; Geiger, M.; Linkhorst, J.; Wessling, M. Transport and clogging dynamics of flexible rods in pore constrictions. *Soft Matter* **2024**, *20*, 6767–6778. [CrossRef] [PubMed]
38. Ge, Y.; Zhang, L.X.; Han, D.D.; Jin, J.M.; Fu, W. Determination and analysis of mechanical properties and morphological characteristics of safflower filaments during harvest. *J. Agric. Mech. Res.* **2015**, *37*, 168–171. [CrossRef]
39. Zhang, Z.G.; Zeng, C.; Xing, Z.Y.; Xu, P.; Guo, Q.F.; Shi, R.M.; Wang, Y.Z. Discrete element modeling and parameter calibration of safflower biomechanical properties. *Int. J. Agric. Biol. Eng.* **2024**, *17*, 37–46. [CrossRef]
40. Liang, Y.Q.; Tang, Z.; Zhang, H.; Li, Y.M.; Ding, Z.; Su, Z. Cross-flow fan on multi-dimensional airflow field of air screen cleaning system for rice grain. *Int. J. Agric. Biol. Eng.* **2022**, *15*, 223–235. [CrossRef]
41. Liang, R.Q.; Chen, X.G.; Zhang, B.C.; Wang, X.Z.; Kan, Z.; Meng, H.W. Calibration and test of the contact parameters for chopped cotton stems based on discrete element method. *Int. J. Agric. Biol. Eng.* **2022**, *15*, 1–8. [CrossRef]
42. Zhang, Q.; Fang, H.; Xu, G.; Niu, M.; Li, J. Experimental and numerical analysis of straw motion under the action of an anti-blocking mechanism for a no-till maize planter. *Agriculture* **2024**, *14*, 1001. [CrossRef]
43. Yuan, H.; Wang, H.; Huang, J.; Li, L.; Peng, S.; Wang, J. Study on uniformity of linear vibrating rice feeding device with matrix-designed outlets based on discrete element method. *J. Food Eng.* **2024**, *381*, 112170. [CrossRef]
44. Coetzee, C.J.; Scheffler, O.C. Review: The calibration of DEM parameters for the bulk modelling of cohesive materials. *Processes* **2023**, *11*, 5. [CrossRef]
45. Fang, W.; Wang, X.; Zhu, C.; Han, D.; Zang, N.; Chen, X. Analysis of film unloading mechanism and parameter optimization of air suction-type cotton plough residual film recovery machine based on CFD–DEM coupling. *Agriculture* **2024**, *14*, 1021. [CrossRef]
46. Shih, T.H.; Liou, W.W.; Shabbir, A.; Yang, Z.; Zhu, J. A new *k*–ε eddy viscosity model for high Reynolds number turbulent flows. *Comput. Fluids* **1995**, *24*, 227–238. [CrossRef]
47. Launder, B.E.; Spalding, D.B. The numerical computation of turbulent flows. *Comput. Methods Appl. Mech. Eng.* **1974**, *3*, 269–289. [CrossRef]

Disclaimer/Publisher's Note: The statements, opinions and data contained in all publications are solely those of the individual author(s) and contributor(s) and not of MDPI and/or the editor(s). MDPI and/or the editor(s) disclaim responsibility for any injury to people or property resulting from any ideas, methods, instructions or products referred to in the content.